Front. Earth Sci. 2019, 13(4): 744–757
https://doi.org/10.1007/s11707-019-0769-5

RESEARCH ARTICLE

Impact of physical representations in CALMET on the simulated wind field over land during Super Typhoon Meranti (2016)

Sui HUANG[1,2], Shengming TANG (✉)[2], Hui YU[2,3], Wenbo XUE[1,2], Pingzhi FANG[2], Peiyan CHEN[2,4]

1 Chinese Academy of Meteorological Sciences, Beijing 100081, China
2 Shanghai Typhoon Institute, China Meteorological Administration, Shanghai 200030, China
3 Key Laboratory of Numerical Modeling for Tropical Cyclones China Meteorological Administration, Shanghai 200030, China
4 The Joint Laboratory for Typhoon Forecasting Technique Applications between Shanghai Typhoon Institute and Wenzhou Meteorological Bureau, Wenzhou 325000, China

Abstract A WRF (Weather Research and Forecasting Model)/CALMET (California Meteorological Model) coupled system is used to investigate the impact of physical representations in CALMET on simulations of the near-surface wind field of Super Typhoon Meranti (2016). The coupled system is configured with a horizontal grid spacing of 3 km in WRF and 500 m in CALMET, respectively. The model performance of the coupled WRF/CALMET system is evaluated by comparing the results of simulations with observational data from 981 automatic surface stations in Fujian Province. The root mean square error (RMSE) of the wind speed at 10 m in all CALMET simulations is significantly less than the WRF simulation by 20%–30%, suggesting that the coupled WRF/CALMET system is capable of representing more realistic simulated wind speed than the mesoscale model only. The impacts of three physical representations including blocking effects, kinematic effects of terrain and slope flows in CALMET are examined in a specified local region called Shishe Mountain. The results show that before the typhoon landfall in Xiamen, a net downslope flow that is tangent to the terrain is generated in the west of Shishe Mountain due to blocking effects with magnitude exceeding 10 m/s. However, the blocking effects seem to take no effect in the strong wind area after typhoon landfall. Whether being affected by the typhoon strong wind or not, the slope flows move downslope at night and upslope in the daytime due to the diurnal variability of the local heat flux with magnitude smaller than 3 m/s. The kinematic effects of terrain, which are speculated to play a significant role in the typhoon strong wind area, can only be applied to atmospheric flows in stable conditions when the wind field is quasi-nondivergent.

Keywords physical representations, CALMET, wind field, Super Typhoon Meranti

1 Introduction

Although tropical cyclones are natural disasters usually leading to huge economic losses and life casualties, the associated wind and rain also have positive implications in alleviating the drought and contributing to the wind energy potential (Lam et al., 2012). Forecasting and reproducing the near-surface typhoon wind field are important in applications such as civil engineering, air pollutant dispersion and wind energy potential assessment. In fact, the accurate assessment of wind energy potential calls for developing better methods of producing high-resolution wind fields, especially over complex terrain.

Traditionally, numerical weather prediction (NWP) models, especially mesoscale area-limited models such as the well-known Regional Atmospheric Modeling system (RAMS; Pielke, et al., 1992), the Eta Model (ETA; Black, 1994), the fifth-generation nonhydrostatic Pennsylvania State University–National Center for Atmospheric Research Mesoscale Model (MM5; Grell et al., 1995) and Weather Research and Forecasting Model (WRF; Skamarock et al., 2008), are used for the purpose of calculating the high-resolution typhoon wind fields over a limited domain. However, these limited area models have limitations due to simplification in physics, and uncertainty in the initial state, lateral boundary conditions and surface

Received October 28, 2018; accepted March 22, 2019

E-mail: tangsm@typhoon.org.cn

characteristics (Al-Yahyai et al., 2010). In addition, when the horizontal grid spacing drops to ~1 km, which is comparable to the typical boundary layer depth and known as terra incognita (Wyngaard, 2004) or model gray zone (Arakawa et al., 2011), neither planetary boundary layer (PBL) schemes nor turbulence closures in NWP models are appropriate to represent the convective vortices. In this regard, notwithstanding the fact that NWP models are widely applied for operational weather forecasts, diagnostic models are still indispensable due to their fast calculation and high accuracy in local regions (Wang et al., 2008). Common examples of diagnostic models are the Wind Atlas Analysis and Application Program (WAsP; Mortensen and Landberg, 1993), California Meteorological Model (CALMET; Scire et al., 1998) and US Environmental Protection Agency (EPA)'s Regular Meteorological Preprocessor Programs (AERMET; US EPA, 2004).

More recently, the hybrid approach combining a mesoscale prognostic model with a diagnostic meteorological model is increasingly being used to generate high-resolution wind fields. Generally, the mesoscale model solves the dynamic primitive equations with horizontal grid spacing of several kilometers, and the diagnostic model is based on continuity equation with much finer resolution to address smaller-scale topographic effects (Ludwig et al., 2006). One of the most prominent example is the WRF/CALMET coupling system. Lu et al. (2012) evaluated the high-resolution wind fields over an island using the hybrid WRF/CALMET approach and found that the overall performance of the WRF/CALMET system is good in simulating high-resolution wind fields in areas of complex terrain. Gioli et al. (2014) compared the aircraft observations of wind speed along the flight track in a long time period with the output from WRF/CALMET model in central Italy. They noted that the coupled WRF/CALMET system has better performance in inland areas than coastal areas, and the diurnal variability in all regions is properly represented. Gonzalez et al. (2015) nested CALMET model to WRF simulations over complex terrain as well as coastal areas in the north-west of Spain. They found that CALMET model provides more accurate PBL depth than the WRF model.

The above studies have illustrated the effectiveness of the coupled WRF/CALMET system as a tool for analyzing the high-resolution wind fields. However, since relatively little has been studied about the physical representations in CALMET in unstable weather conditions such as typhoons so far, the complex terrain poses significant challenges to researchers who wish to analyze the terrain effects with diagnostic models. In this study, a series of numerical simulations of the wind field over land during the process of Super Typhoon Meranti (2016) as seen in the coupled WRF/CALMET simulations are presented. The main goal of the present work is to evaluate the model performance and mechanism of physical representations including blocking effects, kinematic effects of terrain and slope flows over complex terrain during the typhoon process.

The remainder of the article is structured as follows. Section 2 gives an overview of Super Typhoon Meranti in 2016. Section 3 gives a description of the experimental design and the observational data being used to validate the model simulation. Section 4 describes the assessment of the model performance including an overall evaluation, the evaluation for strong winds when affected by Typhoon Meranti, and the evaluation for some specific sites in a local region. Section 5 further examines the impact of different physical representations in CALMET on the gridded wind field in a specified local region. The main discussion and conclusions are summarized in Section 6.

2 Overview of Super Typhoon Meranti (2016)

Super Typhoon Meranti was among the strongest typhoons in the year of 2016. It formed as a tropical depression to the west of Guam island on September 9 and strengthened into typhoon status around 0600 UTC (Universal Time Coordinated) on September 11. During the following day, it moved north-westwards and intensified rapidly into super typhoon status. Super Typhoon Meranti peaked in intensity around 1200 UTC on September 13 when moving through the Luzon Strait. Shortly afterwards, it passed the south of Taiwan island and started weakening steadily as a result of interaction with land surface. Around 1900 UTC on September 14 (0300 CST[1)] on September 15), Meranti made landfall in Xiamen of Fujian Province. After landfall, Meranti weakened dramatically to tropical storm status only within six hours. Since then Meranti gradually weakened over land and from around 0600 UTC on September 15 it began to move slowly north-westwards. Two days later on September 17, Meranti dissipated over the Yellow Sea. Figure 1 shows the best-track position of Meranti from September 9 to September 17, and the data set is from the China Meteorological Administration's best-track (BST) database (Ying et al., 2014).

Figure 2 shows time series of the minimum sea-level pressure, $P_{\min}$, and maximum total wind speed at 10 m, $V_{\max}$, of Meranti, obtained from the BST analyses. It can be easily seen from these time series that Super Typhoon Meranti reached its peak intensity at 1200 UTC on September 13 with $P_{\min}$ falling to 890 hPa and $V_{\max}$ up to 75 m/s, which is comparable to those of super typhoon Haiyan in 2013. Around 1900 UTC on September 14, Meranti made landfall in Xiamen as a super typhoon with surface winds up to 52 m/s, which makes it the strongest typhoon on record to impact Fujian Province.

1) China Standard Time (CST) = UTC + 8 hours

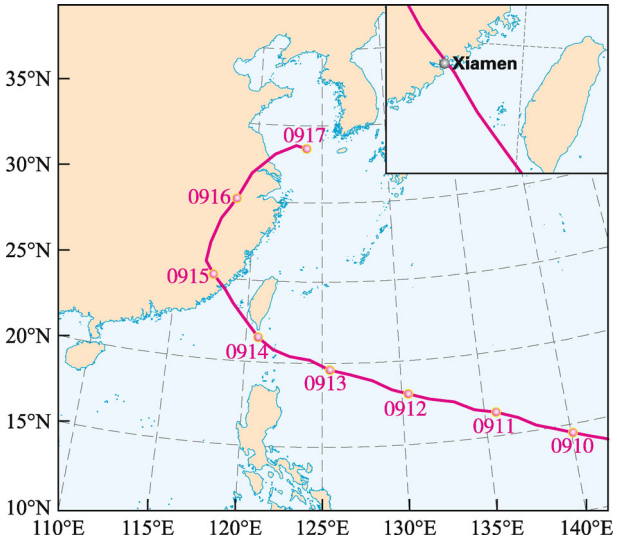

Fig. 1 Best-track position of Meranti (UTC) * landfall in Xiamen

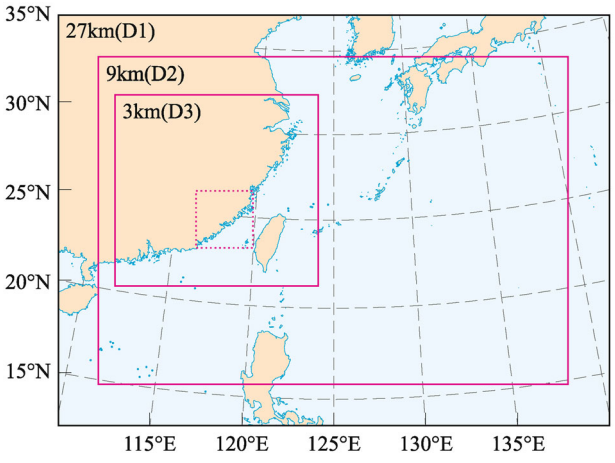

Fig. 3 Area coverage for the three nested domains in the WRF model. The dashed box denotes the computational domain in CALMET.

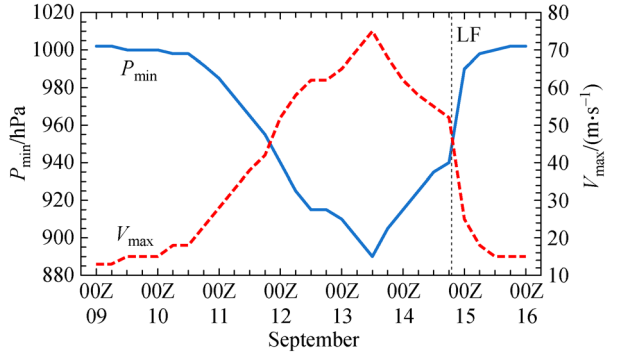

Fig. 2 Time series of the minimum sea-level pressure, P_{min}, and maximum total wind speed at 10 m, V_{max}, of Meranti as seen in the BST analyses. The vertical dashed line marks the time of landfall in Xiamen and the capital letter 'Z' denotes the time of UTC.

3 Experimental design

3.1 Mesoscale model WRF

The mesoscale model used in this study is the WRF model version 3.8.1 and the dynamical solver is the Advanced Research WRF (ARW) core, which is mainly developed by the National Center for Atmospheric Research (NCAR). The model is widely applied for meteorology across scales from meters to thousands of kilometers (Skamarock et al., 2008).

The WRF model is configured using three two-way nested domains with grid spacing of 27, 9 and 3 km, respectively. The center of the outermost domain is located at 25°N, 125°E. The domains have 135 × 203 (D1), 343 × 241 (D2) and 445 × 421 (D3) grid points, respectively (Fig. 3). There are 30 full Eta levels in the vertical direction with 8 levels below 1 km to resolve the detailed structure of the PBL. The pressure on the model top is set to 50 hPa.

The Lin scheme (Lin et al., 1983) is applied in all domains for microphysical parameterization. The Kain-Fritsch cumulus scheme (Kain, 2004) is applied in the outermost domain and no cumulus parameterization is used in the other two domains. The PBL is modeled using the quasi-normal scale elimination PBL scheme (Sukoriansky et al., 2005) and the Noah land surface model (Chen and Dudhia, 2001) is used. Both shortwave and longwave radiation processes are parameterized using the new version of the rapid radiative transfer model (Iacono et al., 2008). The topographic data were obtained from the US Geological Survey (USGS) global 30 arc-seconds elevation (GTOPO30) data set, and the 21-category Moderate Resolution Imaging Spectroradiometer (MODIS)-based land use data were used to determine the physical properties of the land surface.

The initial and boundary conditions are provided by the NCEP-GFS (National Centre for Environmental Prediction-Global Forecasting System) analyses four times a day with horizontal grid spacing of 1.0 degree. All domains start integration at 0000 UTC on September 11 and run for 120 h. The results are examined at time intervals of 1 h.

3.2 Diagnostic model CALMET

The diagnostic model used herein is the California Meteorological Model (CALMET) version 6.5, which is the meteorological component of the California Puff (CALPUFF) dispersion model (Scire et al., 1998). The diagnostic CALMET model computes the wind field within two steps. In the first step, an initial guess wind field is produced by applying kinematic effects of terrain, blocking effects and slope flows. In the second step, an objective analysis procedure is adopted to introduce the

observational data into the initial guess wind field. In the present configuration, the initial guess wind field is obtained from the outputs of WRF innermost domain with horizontal grid spacing of 3 km (Fig. 3). In this study, the objective analysis procedure is not used and only the wind field in the first step is concerned for the evaluation of terrain adjustment.

The Lambert Conformal Conic (LCC) projection system is used in CALMET and the computational domain is set up with only one domain having 745 × 745 grid points with grid spacing of 500 m (Fig. 4). Altogether there are 17 levels in the vertical direction, including 10, 30, 50, 70, 90, 110, 130, 150, 170, 190, 300, 500, 750, 1000, 1500, 2500 and 3500 m.

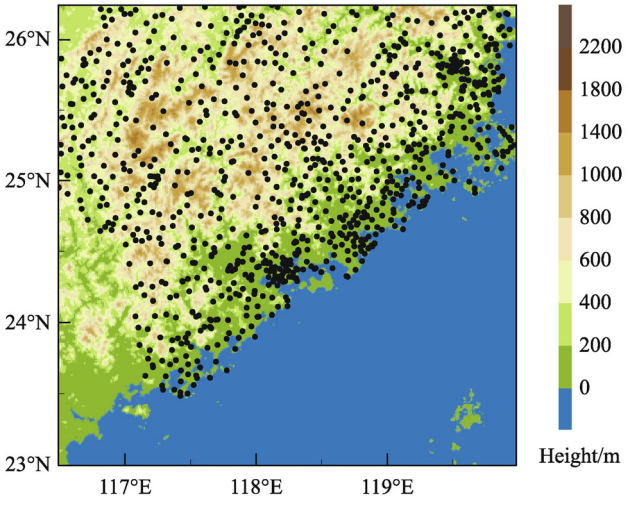

Fig. 4 Computational domain in CALMET (area in the dashed box shown in Fig. 3). The shaded contours represent the terrain elevations and the automatic surface observational stations are marked by solid dots.

The topographic data in CALMET is obtained from the National Aeronautics and Space Administration (NASA) Shuttle Radar Topography Mission (SRTM) global 90 m digital elevation data set, and USGS's Global Land Cover Characterization (GLCC)-based land use data are applied to determine the surface physical properties. As shown in Fig. 4, the topographic features in CALMET are more detailed as the gird spacing decreases from 3 km to 500 m, thus the diagnostic computations could be regarded as an attempt to compensate for the difference between the mesoscale model and the actual terrain elevations (Lu et al., 2012).

The physical representations used in the computation include blocking effects, kinematic effects of terrain and slope flows. CALMET parameterizes the thermodynamic blocking effects of terrain using the term of the local Froude number (Allwine and Whiteman, 1985). The kinematic effects of terrain are parameterized using an iterative divergence-minimization approach of Liu and Yocke (1980). Slope flows are calculated based in terms of distance to the crest, terrain slope and local sensible heat flux (Mahrt, 1982). In the calculations to be described, we examine the impact of physical representations on the simulated wind field of Typhoon Meranti. Altogether, eight simulations are presented by different combination of the above three physical representations including blocking effects, kinematic effects of terrain and slope flows, which are detailed in Table 1.

Table 1 Eight simulations in CALMET

Symbol	Blocking effects	Kinematic effects	Slope flows
CAL0	√	×	√
CAL1	√	√	√
CAL2	√	√	×
CAL3	×	√	√
CAL4	√	×	×
CAL5	×	√	×
CAL6	×	×	√
CAL7	×	×	×

All simulations (CAL0–CAL7) start at 2100 UTC on September 13 and run for 48 h. The results are examined at time intervals of 1 h.

3.3 Observational data

The observational data are collected from 981 automatic surface observational stations over the computational domain in CALMET (Fig. 4). The wind speed, wind direction and air temperature are recorded as an integrated average every 5 min at a height of 10 m from the surface. All the data collection, processing and storage meet the requirements of the national standard GB/T 35237-2017. The hourly averaged records are used as validation data. Both the observed and simulated time series cover the period from 2100 UTC on September 13 to 2000 UTC on September 15. As the automatic observational stations cover most of the strong wind areas when Typhoon Meranti made landfall, it is reasonable to expect that the observational data herein is capable of validating the surface wind field structure of the numerical simulations.

4 Results of WRF/CALMET simulations

4.1 Overview of WRF simulation

An overview of the vortex development in the WRF simulation is first presented. Figure 5(a) shows the comparison of typhoon track in both BST analyses and WRF simulation. Figure 5(b) and Fig. 5(c) show P_{min} and V_{max} respectively. The vortex center here is defined as the

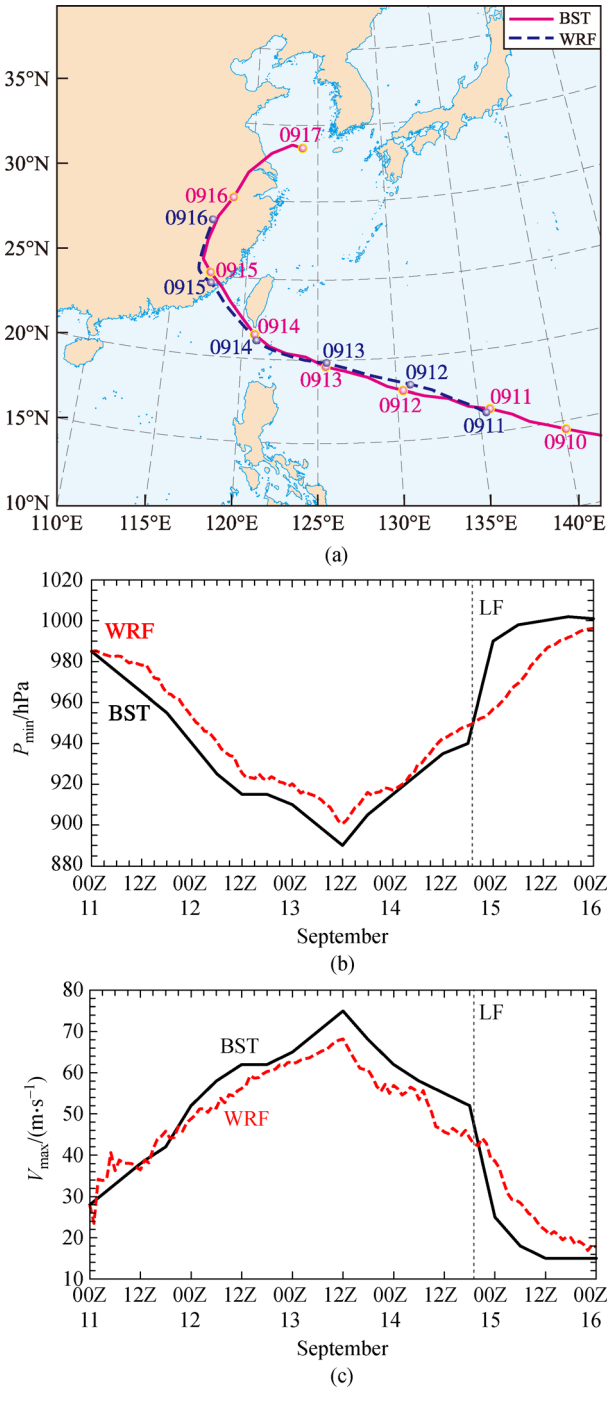

Fig. 5 Vortex development in both BST analyses and WRF simulation. Time series of (a) track, (b) P_{min}, and (c) V_{max}. The vertical dashed line marks the time of landfall in Xiamen.

location of P_{min}.

In the BST analysis, Typhoon Meranti made landfall around 1900 UTC on September 14 in Xiamen while in the WRF simulation, the landfalling time is about two hours later, indicating that the vortex moves slower during the day of September 14. In general, the typhoon track in the WRF simulation satisfactorily fits that in the BST analysis.

After initialization at 0000 UTC on September 11, the vortex in WRF simulation decays slightly during the first hour and then intensifies rapidly during the next four hours. Thereafter V_{max} decays gradually in the next 7 h to about 37 m/s, which is close to the value in the BST analysis. Following the adjustment phase of 14 h, V_{max} increases gradually during the next two days to peak at 68 m/s. Before the time of landfall in Xiamen, the agreement of P_{min} and V_{max} between the WRF simulation and the BST analyses is remarkably good. The vortex in the BST analysis undergoes a rapid weakening phase after landfall while V_{max} decreases more slowly in the WRF calculation. The rapid weakening of Meranti after landfall is presumably because its warm and moist core disappears fast and the horizontal range of positive vorticity column decreases gradually (Zhao et al., 2018).

In general, the typhoon track, the values of P_{min} and V_{max} in the WRF simulation fit those in the BST analyses well. The gridded wind fields generated by the WRF innermost domain (D3 in Fig. 3) will provide the initial guess wind field in CALMET.

4.2 CALMET simulation

The performance of physical representations in CALMET is mainly evaluated by validating the wind speed simulations with observations. Parameters including wind speed, wind direction and air temperature from the CALMET simulations are compared with those from automatic observational stations.

4.2.1 Overall wind fields comparison

The assessment of physical representations is organized beginning from overall comparisons in Fujian Province. Figure 6 shows the time series of the root mean square error (RMSE) and correlation coefficient (COR) for 10-m wind speed, V_{10}, wind direction, WD_{10}, and air temperature, T_{10}, in both WRF simulation and CALMET simulations CAL0 to CAL7 over the whole computational domain (Fig. 4). The vertical dashed line marks the time of landfall in WRF simulation at 2100 UTC on September 14 (0500 CST on September 15), which is about two hours later than that of BST analyses (Fig. 5(a)). The inverse square law of distance is used to interpolate the gridded data in numerical calculations into the places of observational stations. The comparison starts at 2100 UTC on September 13 and ends at 2000 UTC on September 15.

A prominent feature of overall comparisons is that the RMSE of V_{10} in each CALMET simulation varies between 3 m/s and 10 m/s and is significantly less than the WRF simulation by 20%–30% (Fig. 6(a)), which means the coupled WRF/CALMET system does provide more realistic simulated wind speed. After the typhoon landfall in Xiamen, the COR of V_{10} in both WRF and CALMET

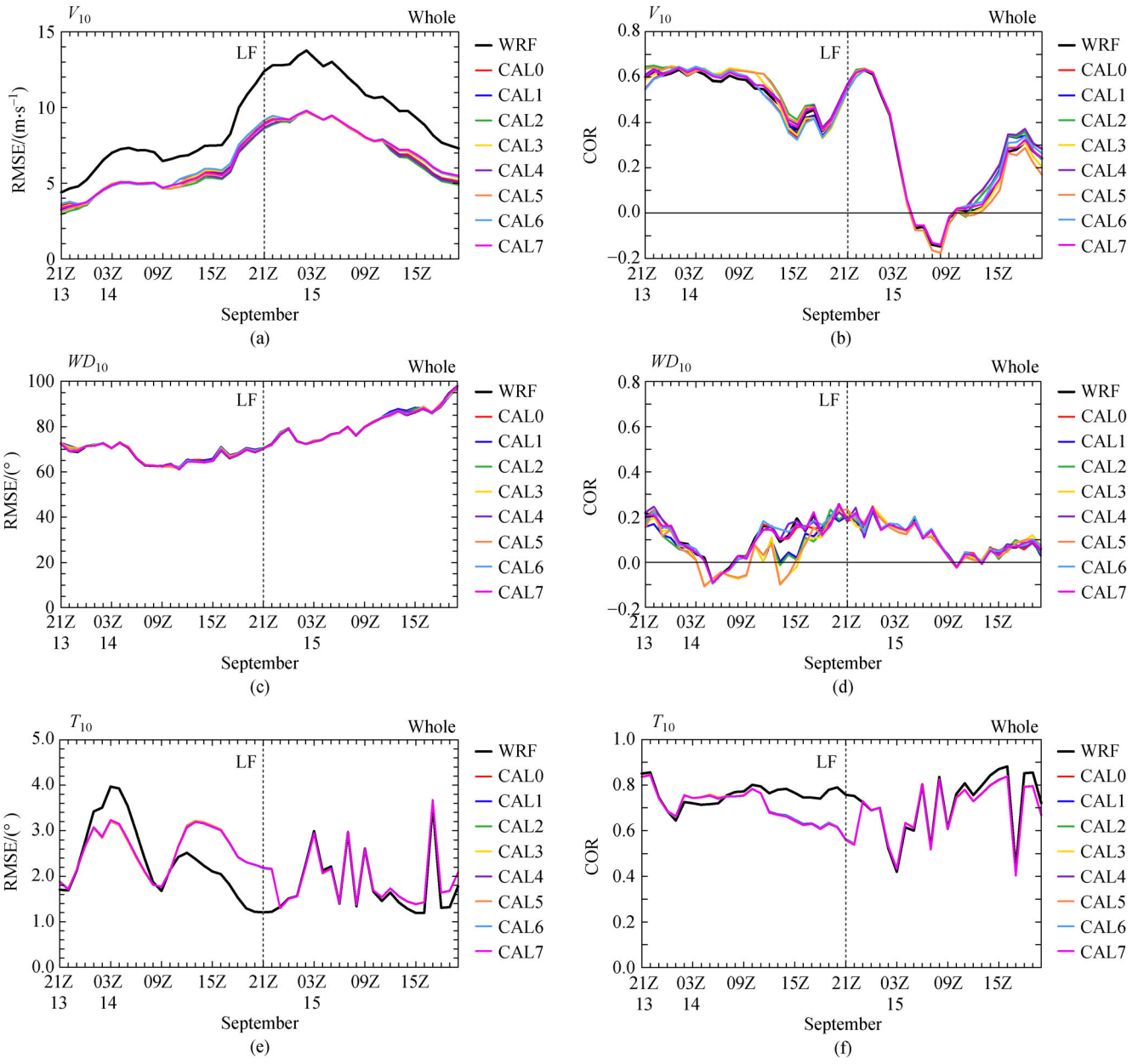

Fig. 6 Time series of RMSE and COR for 10-m (a, b) wind speed, V_{10}, (c, d) wind direction, WD_{10}, and (e, f) air temperature, T_{10}, in both WRF simulation and CALMET simulations CAL0 to CAL7 over the whole computational domain. The vertical dashed line marks the time of landfall in Xiamen.

simulations decreases rapidly and even attains negative values (Fig. 6(b)), which is presumably because the WRF simulation fails to capture the rapid weakening phase of Typhoon Meranti after landfall. Decreasing the grid spacing from 3 km in WRF to 500 m in CALMET provides more detailed topographic features, but there are no corresponding improvements indicated by the RMSE and COR for WD_{10} (Figs. 6(c), 6(d)), leading to the counterintuitive fact that wind simulations do not improve the wind direction with higher horizontal resolution in general. Over land, the three-dimensional temperature field is calculated based on upper air and surface temperature data and an estimation of the convective mixing depth (Holtslag and Ulden, 1983). As shown in Fig. 6(e) and Fig. 6(f), the RMSE and COR of T_{10} in CALMET are comparable to those in WRF.

4.2.2 Typhoon strong wind fields comparison

Now we focus on the comparison of the typhoon strong wind fields with corresponding observations. In this study, the typhoon strong wind area is defined as the area within the radius of gale-force wind ($>$ 17.1 m/s, R17) at a height

of 10 m. Figure 7 shows time series of RMSE for V_{10}, WD_{10} and T_{10} in both WRF simulation and eight CALMET simulations within the radius of the azimuthally averaged wind speed of 17.1 m/s. The shaded areas denote the number of surface observational stations within R17 at each time point. The comparison starts at 1400 UTC on September 14 and ends at 0900 UTC on September 15, during which the Fujian Province is affected by the strong wind fields of Typhoon Meranti.

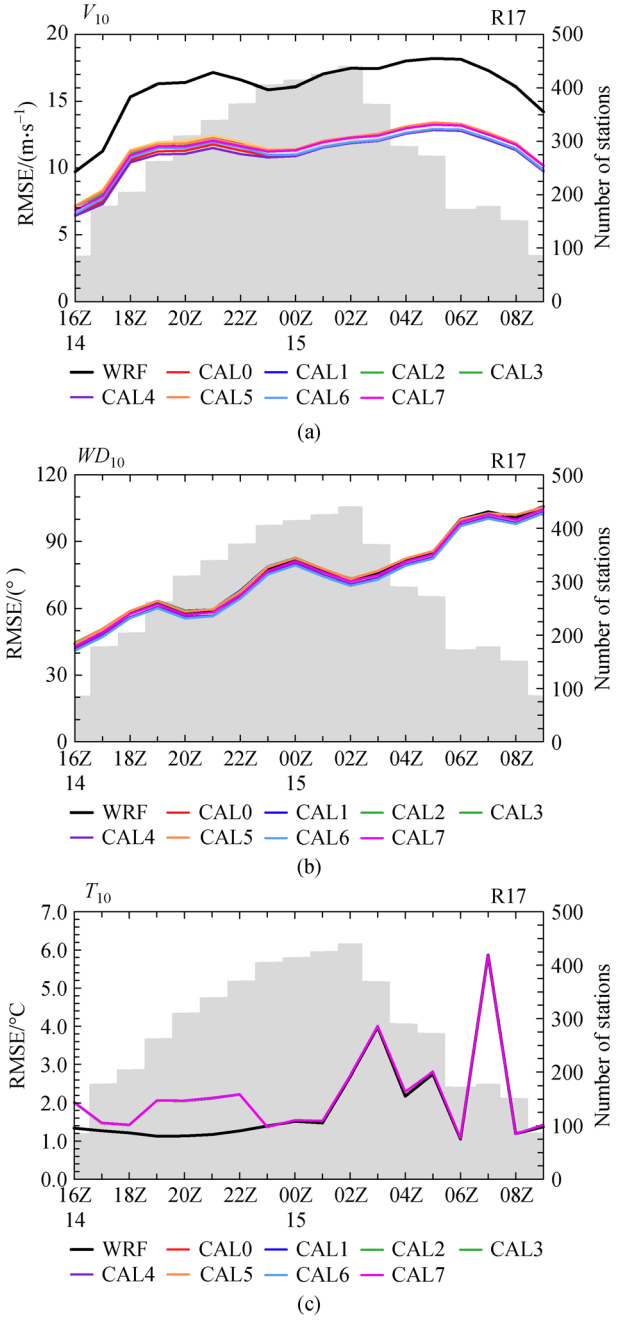

Fig. 7 Time series of RMSE for (a) V_{10}, (b) WD_{10}, and (c) T_{10} in both WRF simulation and CALMET simulations CAL0–CAL7 within R17. The shaded areas denote the number of surface observational stations within R17 at each time point.

Interestingly, the behavior of RMSE for V_{10}, WD_{10} and T_{10} in the typhoon strong wind area (Fig. 7), to some extent, are similar to those in the whole computational domain (Fig. 6), indicating that physical representations in CALMET are insensitive to the value of wind speed. This result is mainly because CALMET is only a diagnostic model and does not solve the dynamic and thermodynamic equations. A significant feature of comparisons within R17 is that the RMSE of V_{10} in each CALMET simulation fluctuates between 6 m/s and 13 m/s, which is remarkably less than the WRF simulation by 20%–30% (Fig. 7(a)), supporting the idea that the coupled WRF/CALMET system is capable of representing more realistic topographic driven patterns in the typhoon strong wind area. In contrast, the behavior of RMSE for WD_{10} and T_{10} is quite similar to those in WRF (Fig. 7(b), 7(c)), indicating that the wind direction and air temperature in CALMET are mainly determined by the initial guess field from WRF output.

Significantly, inspection of both Fig. 6 and Fig. 7 suggests that there is no systematic difference in the behavior of RMSE or COR between eight CALMET simulations, indicating that these three physical representations have little impact on the simulated wind field and temperature near the surface. This result is presumably because the overall performance of the CALMET model may be contributed by the objective analysis procedure, rather than the physical adjustments for the finescale terrain effects (Yim et al., 2007). As the comparison is over the whole computational domain (Fig. 6) or in the typhoon strong wind area (Fig. 7), it is reasonable to speculate that the impact of physical parametrizations would be larger in a relative small local area such as a mountainous area with complex terrain, which will be discussed in the next section.

4.2.3 Comparison at Shishe Mountain

Investigating the spatial distribution and variability of the simulated wind field is important because one of the major benefits of the coupled WRF/CALMET system is for capturing the effects of finer scale terrain on the wind field (Lu et al., 2012). Now we focus on the performance of physical representations in a selected local area. Figure 8 shows the terrain elevations of Shishe Mountain and surrounding areas. The peak of Shishe Mountain, which is about 50 km north of Xiamen, is located at 118.186°E, 24.905°S with an altitude of 1118 m above sea level. Altogether, 12 automatic surface observational stations are located in this local area.

Figure 9 shows time series of V_{10} and WD_{10} in both WRF and CALMET simulations and observed at Station 1, Station 4 and Station 5. The observational Stations 1 and 4 are located in the north and south of Shishe Mountain, respectively, and Station 5 is located near the mountain top

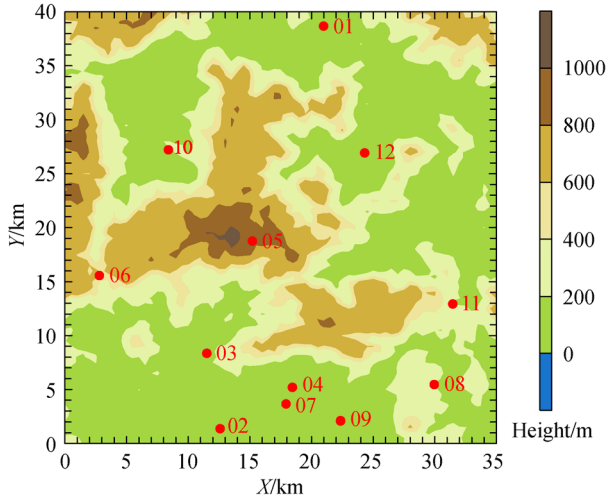

Fig. 8 Shishe Mountain and surrounding areas. The shaded contours represent the terrain elevations and the automatic surface observational stations are marked by solid dots.

(Fig. 8). The vertical dashed line marks the time of landfall in the WRF simulation at 2100 UTC on September 14. The comparison covers the whole CALMET calculation period starting from 2100 UTC on September 13 to 2000 UTC on September 15. Inspection of Fig. 9 suggests that the values of V_{10} in eight CALMET simulations are generally closer to observations than the WRF simulation, supporting the idea that the coupled WRF/CALMET system represents more realistic simulated wind speed than the mesoscale model only. Likewise, the behavior of WD_{10} in CALMET is similar to that in WRF, indicating that the coupled system is not capable of improving wind direction with decreasing grid spacing.

Before the landfall of Typhoon Meranti, the prevalent wind pattern is defined by the north-east wind and V_{10} at Station 5 is around 10 m/s, which is larger than that in Station 1 and Station 4. This result is mainly due to the blocking effects on the upwind and downwind side of Shishe Mountain. When the inner core region of Typhoon Meranti is passing through the Shishe Mountain at around 0000 UTC on September 15, the prevalent wind directions for these three stations are rapidly turning into south-east wind as shown in the CALMET simulations CAL0–CAL7. Interestingly, the wind speed exhibits significant spatial variation characterized by wind speed maxima around the hilltops associated with slope flows. The maximum V_{10} at Station 5 is up to 22 m/s, while the wind speed maxima is 23 and 28 m/s at Station 1 and Station 4, respectively. This is mainly because Station 5 is affected by the blocking effects with south-west wind while Station 1 and Station 4 are hardly affected with south-east wind or south wind. In general, these results indicate that CALMET shows great skill at deriving local structure of wind field in a complex terrain.

Inspection of Fig. 9 suggests that the impact of different physical representations on surface wind fields in a local area is comparably larger than that over the whole computational domain (Fig. 6) or typhoon strong wind area (Fig. 7). As seen from the behavior of V_{10} at three stations, a systematic difference exists in eight CALMET simulations that could be divided into two groups accordingly. Group 1 contains experiments CAL0, CAL4, CAL6 and CAL7, and Group 2 contains experiments CAL1, CAL2, CAL3 and CAL5. Significantly, V_{10} in Group 1 is systematically larger than that in Group 2 by 10%–20% at Station 5 (Fig. 9(e)), and some systematic differences can also be detected at Station 1 and Station 4 (Figs. 9(a), 9(c)).

Figure 10 shows time series of RMSE for V_{10} and WD_{10} in both WRF simulation and CALMET simulations CAL0–CAL7 at Shishe Mountain. The comparison starts at 2100 UTC on September 13 and ends at 2000 UTC on September 15. Inspection of Fig. 10 shows a common feature with the above findings that the RMSE of V_{10} in each CALMET simulation is significantly less than the WRF simulation while there is no corresponding improvement indicated by the RMSE of WD_{10}. It is noteworthy that measurable difference exists in the RMSE between eight CALMET simulations, indicating that different combination of physical representations will produce different wind structure in a local mountainous area.

To quantify the differences between eight CALMET simulations at Shishe Mountain, the time averaged RMSE for V_{10} and WD_{10} in both the WRF simulation and CALMET simulations CAL0–CAL7 are calculated as detailed in Table 2. Interestingly, the values of time averaged RMSE for V_{10} and WD_{10} in Group 1, which contains experiments CAL0, CAL4, CAL6 and CAL7, are larger than those in Group 2 by approximately 10% except experiment CAL7. Referring back to Table 1, the common feature of the experiments in Group 1 is that the kinematic effects of terrain are not included. Inspection of Table 2 as well as Table 1 suggests that the blocking effects and slope flows are effective in dealing with complex terrain in the diagnostic model, while the kinematic effects of terrain seem to make the numerical results worse.

5 Physical representations

5.1 Blocking effects

In CALMET, the thermodynamic blocking effects are parameterized by using the term of the local Froude number (Allwine and Whiteman, 1985):

$$Fr = \frac{V}{N\Delta h_t}, \tag{1}$$

where Fr is the local Froude number, V is the local wind

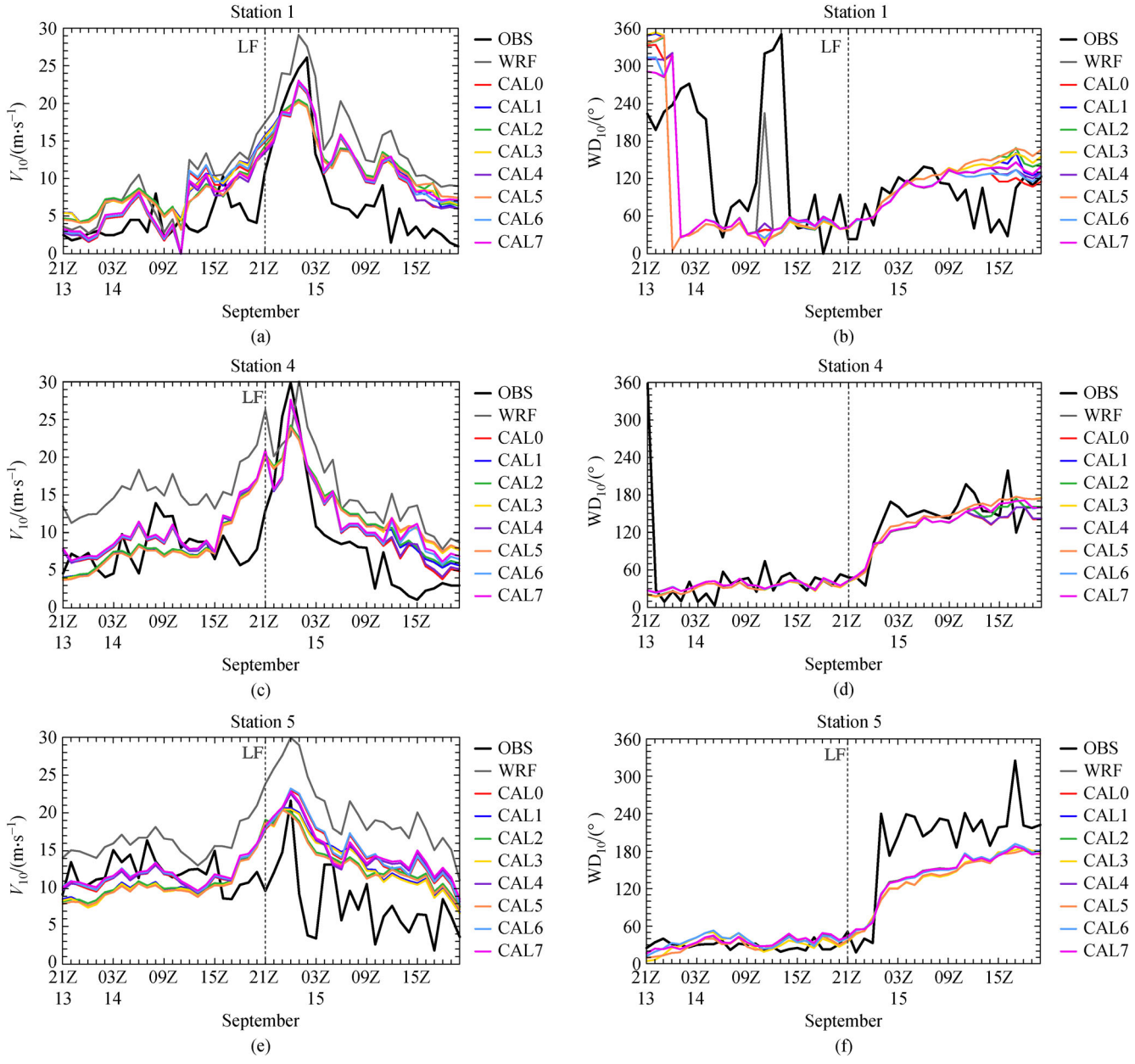

Fig. 9 Time series of V_{10} and WD_{10} in both WRF and CALMET simulations observed at Station 1 (a, b), Station 4 (c, d) and Station 5 (e, f). The vertical dashed line marks the time of landfall in Xiamen.

speed, N is the Brunt-Väisälä frequency, and Δh_t is an effective obstacle height. The Froude number is calculated at each grid point. If Fr is smaller than a critical Froude number and wind flows move uphill, CALMET adjusts the wind direction to be tangent to the terrain and keeps the wind speed unchanged. On the contrary, there will be no adjustment for the wind flow if Fr is larger than the critical Froude number. The default value of the critical Froude number is set to 1.0.

As the near-surface wind speed and atmospheric stability change rapidly when Typhoon Meranti passes through the area of Shishe Mountain, it is reasonable to calculate Fr inside and outside the typhoon strong wind area. In this study, the typhoon strong wind area is defined as the area within the radius of gale-force wind (R17) at the height of 10 m. Figure 11 shows the time-averaged Fr and differences of wind vectors at 10 m inside and outside R17 of Typhoon Meranti at Shishe Mountain. To exclude the interference of the numerical model itself, the differences are calculated by subtracting the wind vectors of CAL7 from those of CAL4 to represent the pure impact of blocking effects on the wind field near the surface.

The comparison of Fig. 11(a) and Fig. 11(b) suggests that the value of Fr is much larger when Shishe Mountain

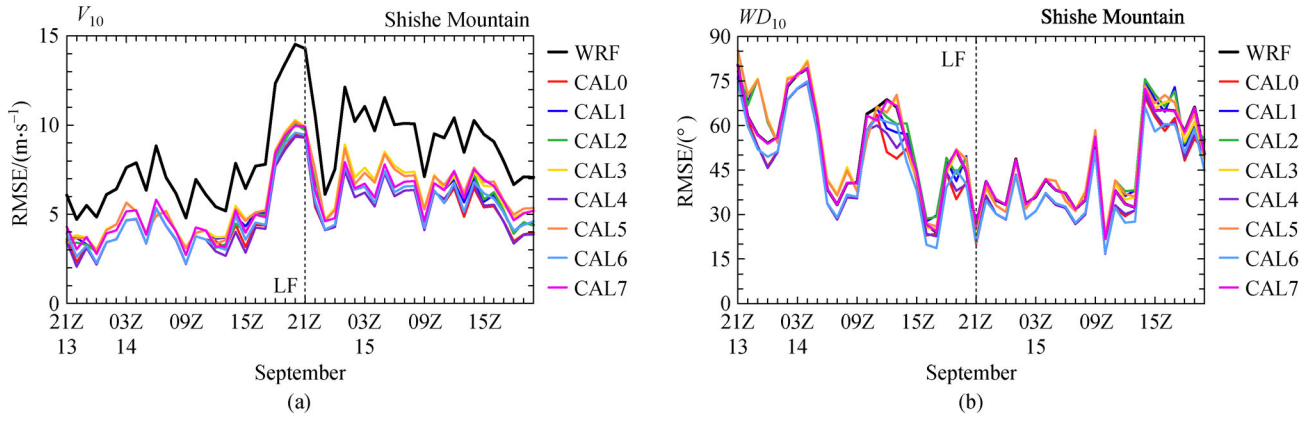

Fig. 10 Time series of RMSE for (a) V_{10} and (b) WD_{10} in both WRF simulation and CALMET simulations CAL0–CAL7 at Shishe Mountain. The vertical dashed line marks the time of landfall in Xiamen.

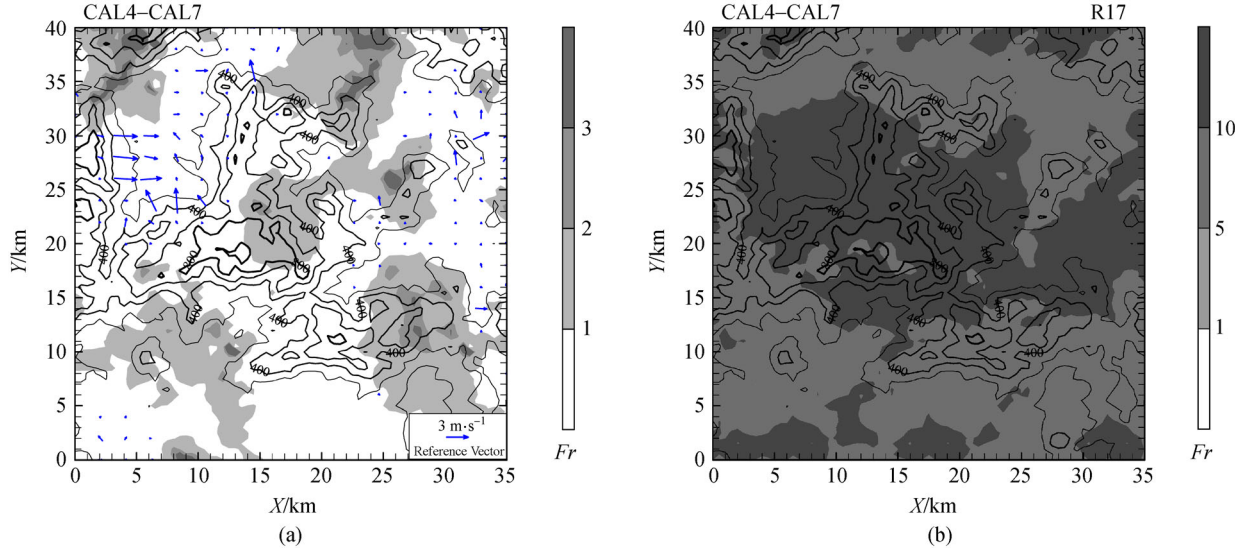

Fig. 11 Local Froude number (filled contours) and differences of wind vectors at 10 m, time averaged during (a) 1500 to 2000 UTC on September 14 and (b) 2200 UTC on September 14 to 0300 UTC on September 15. The differences are calculated by subtracting the wind vectors of CAL7 from those of CAL4. The contour line denotes the terrain height of Shishe Mountain.

Table 2 Time averaged RMSE for V_{10} and WD_{10} in both WRF simulation and CALMET simulations CAL0–CAL7 at Shishe Mountain during the whole CALMET calculation period from 2100 UTC on September 13 to 2000 UTC on September 15.

Symbol	Mean RMSE for V_{10}/(m·s^{-1})	Mean RMSE for WD_{10}/(°)
WRF	8.40	49.45
CAL0	5.00	44.31
CAL1	5.70	50.34
CAL2	5.62	50.66
CAL3	5.86	50.36
CAL4	4.90	44.56
CAL5	5.83	50.68
CAL6	5.14	44.18
CAL7	5.59	49.40

is located within R17, which is mainly because the wind speed (V) increases and atmospheric stability (N) decreases in the typhoon strong wind area. As the value of Fr exceeds the critical Froude number (1.0) at every grid point, no adjustment is made to the wind field within R17 (Fig. 11b). As seen from Fig. 9, the prevailing wind at Shishe Mountain during the period from 1500 to 2000 UTC on September 14 is north-east wind, which tends to be blocked by the hills in the west and north part. When Fr is smaller than 1.0, a net downslope flow that is tangent to the terrain is generated in the west of Shishe Mountain due to the blocking effects with its magnitude up to 12 m/s (Fig. 11a). On the whole, the blocking effects in CALMET seem to take no effect in the typhoon strong wind area and only adjust the wind fields outside the strong wind area when Fr is less than 1.0.

5.2 Kinematic effects of terrain

In CALMET, the kinematic effects of terrain are parameterized by the approach of Liu and Yocke (1980). First, the vertical velocity in Cartesian coordinates, w, is calculated as:

$$w = (V \cdot \nabla h_t)\exp\left(-\frac{N}{|V|}z\right), \quad (2)$$

where h_t is the terrain height and z is the vertical coordinate. Then a divergence-minimization procedure described by Goodin et al. (1980) is applied to evaluate the horizontal wind components iteratively:

$$Div = \frac{\partial u}{\partial x} + \frac{\partial v}{\partial y} + \frac{\partial w}{\partial z} < \varepsilon, \quad (3)$$

where Div is the three-dimensional divergence, u and v are the horizontal wind components, and ε is the maximum allowable divergence with the default value of 5×10^{-6}. The maximum number of iterations is set to 50 steps by default.

Figure 12 shows the time-averaged three-dimensional divergence and differences of wind vectors at 10 m inside and outside R17 of Typhoon Meranti at Shishe Mountain. The differences are calculated by subtracting the wind vectors of CAL7 from those of CAL5 to represent the impact of kinematic effects on the near-surface wind field. A prominent feature is that at each grid point Div is much larger than ε, which indicates that the divergence-minimization procedure has not been accomplished within 50 steps. However, even though the maximum number of iterations could be manually extended to a numerous value such as 500 steps, Div is still much larger than ε (not shown), which suggests that the continuity law of air mass cannot be satisfied with the impact of kinematic effects of terrain.

Inspection of Fig. 12 also suggests that it does not matter whether the locations is outside or inside R17 of Typhoon Meranti, both patterns of Div and wind vector differences mismatch that of the local terrain, indicating that there is a systematic contamination of wind fields during the typhoon process. This result is presumably because w is computed only by the orographic forcing and the initial guess wind field is assumed to be quasi-nondivergent, which is incorrect under typhoon conditions as the vertical motion is not negligible in the inner core region, especially near the eyewall. As a result, the kinematic effects of terrain in CALMET can only be applied to atmospheric flows in stable conditions when the wind field is quasi-nondivergent. The unstable conditions such as typhoons, tornados and frontal systems are not appropriate to parameterize using the kinematic effects of terrain in CALMET. In other words, the present performance of kinematic effects under very specific weather conditions needs to be improved.

5.3 Slope flows

In CALMET, an empirical scheme based on the shooting flow parameterization of Mahrt (1982) is applied to calculate the effects of slope flows:

$$S = \left[\frac{Q_h g x \sin\alpha}{\rho c_p T(C_D + k)}\right]^{1/3}\left[1 - \exp\left(-\frac{x}{L_e}\right)\right]^{1/3}, \quad (4)$$

where S is wind speed of the slope flow, Q_h is the local sensible flux, g is the gravitational acceleration constant

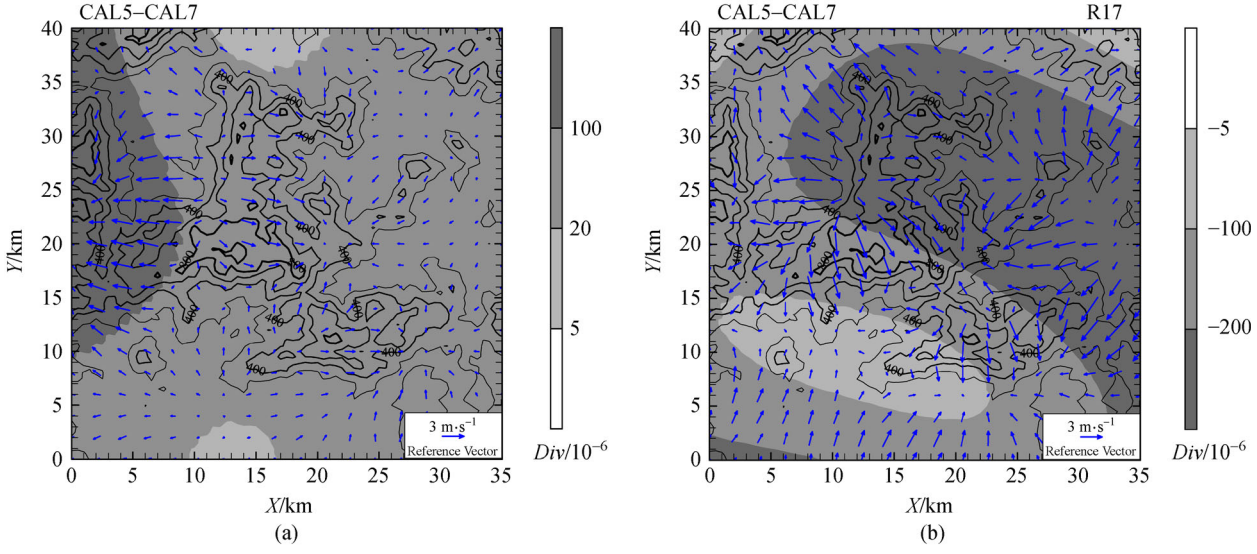

Fig. 12 The divergence (filled contours) and differences of wind vectors at 10 m, time averaged during (a) 1500 to 2000 UTC on September 14 and (b) 2200 UTC on September 14 to 0300 UTC on September 15. The differences are calculated by subtracting the wind vectors of CAL7 from those of CAL5. The contour line denotes the terrain height of Shishe Mountain.

(9.8 m s^{-2}), x is the distance to the crest of the hill, α is the angle of the terrain relative to the horizontal, ρ is the air density, c_p is the specific heat of air, T is the air temperature, C_D is the surface drag coefficient, k is the entrainment coefficient and L_e is an equilibrium length scale.

For downslope flows, values of C_D and k are set to $C_D = k = 0.04$, which are within the range of observed values in vegetation-covered areas (Mahrt, 1982; Horst and Doran, 1986). For upslope flows, larger values of $(C_D + k) \sim 1$ are chosen for considering the resistance due to stratification and then Eq. (4) can be rewritten as:

$$S \cong \left(\frac{Q_h g x \sin\alpha}{\rho c_p T}\right)^{1/3}. \quad (5)$$

For each grid point, x is constant and α relates to the local wind direction. Then it is reasonable to expect that the variation of S is mainly contributed by Q_h. Figure 13 shows time series of Q_h averaged at Shishe Mountain in experiment CAL6. The diurnal signal is a remarkable feature with the peak value up to 260 W/m^2 around 0500 UTC. Another important feature is that Q_h remains nearly constant at night with the value around -50 W/m^2.

Figure 14 shows the time-averaged Q_h and differences of wind vectors at 10 m during the night and daytime at Shishe Mountain. The differences are calculated by subtracting the wind vectors of CAL7 from those of CAL6 to represent the wind speed of the slope flow. The most prominent feature is that the flow moves downslope at night and upslope in the daytime. As the flow moves downslope during the night, it is cooled by the local heat flux ($Q_h < 0$) and the peak value of S is up to 2.5 m/s

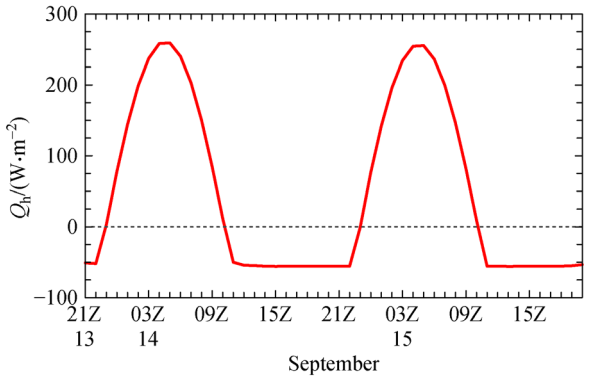

Fig. 13 Time series of the area-averaged Q_h at Shishe Mountain in experiment CAL6.

(Fig. 14a). During the daytime, the flow moves upslope and is warmed by the local heat flux ($Q_h > 0$). However, the slope flow is weaker in the daytime with a maximum speed of approximately 1.5 m/s (Fig. 14b).

The comparison of Fig. 11, Fig. 12 and Fig. 14 shows that during the typhoon process, the blocking effects play a leading role outside the typhoon strong wind area and the associated wind speed difference can exceed 10 m/s. However, in the typhoon strong wind area the blocking effects take no effect and the slope flow is very small with the maximum speed of approximately 1.5 m/s (Fig. 14). As a result, it is reasonable to speculate that the kinematic effects of terrain might play a significant role in the typhoon strong wind area over complex terrain. However, the current physical processes of kinematic effects in CALMET need to be improved.

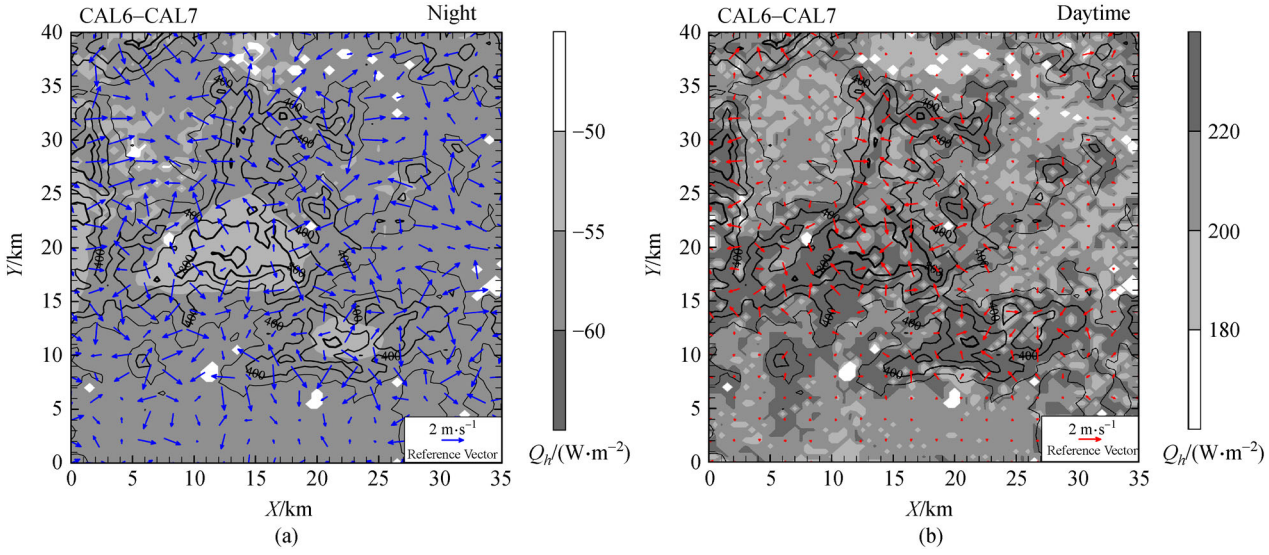

Fig. 14 Local sensible heat flux (filled contours) and differences of wind vectors at 10 m, time averaged during (a) the night (2100 CST on September 14 to 0400 CST on September 15) and (b) the daytime (0900 to 1600 CST on September 15). The differences are calculated by subtracting the wind vectors of CAL7 from those of CAL6. The contour line denotes the terrain height of Shishe Mountain.

6 Conclusions and discussion

We have analyzed the impact of three physical representations in CALMET on the near-surface wind field over land during the period when super Typhoon Meranti made landfall in Fujian Province in 2016. A WRF simulation with a horizontal grid spacing of 3 km together with eight CALMET simulations with a horizontal grid spacing of 500 m were discussed. The differences between eight CALMET simulations were determined by different combination of physical representations including blocking effects, kinematic effects of terrain and slope flows. The model performance of physical representations was evaluated by comparing the results of simulations with observational data from automatic surface stations in Fujian Province.

The impact of different physical representations on the near-surface wind field is shown to be larger in a local area (Shishe Mountain) than that over the whole computational domain or typhoon strong wind area. All comparisons show that the RMSE of the wind speed at 10 m is significantly less than the WRF simulation by 20%–30%, which suggests that the coupled WRF/CALMET system is capable of representing more realistic simulated wind speeds than the mesoscale model only. However, there are no corresponding improvements indicated by the RMSE of wind direction and air temperature. Inspection of the wind field at Shishe Mountain suggests that the blocking effects and slope flows are effective in dealing with complex terrain in the diagnostic model, while the kinematic effects of terrain seem to contaminate the numerical results.

After the assessment of the model performance by traditional verification statistics, the physical process and mechanism of each physical representation that impact the variation of wind fields are investigated at Shishe Mountain. Before the typhoon landfall in Xiamen and when the Froude number is smaller than 1.0, a net downslope flow that is tangent to the terrain is generated in the west of Shishe Mountain due to the blocking effects with its magnitude exceeding 10 m/s. After the typhoon landfall, the blocking effects in CALMET seem to take no effect in the typhoon strong wind area as the Froude number on each grid point is larger than 1.0. Interestingly, whether being affected by the typhoon strong wind or not, the slope flows move downslope at night and upslope in the daytime due to the diurnal variability of the local heat flux. Comparatively, slope flows are weaker in the daytime with the maximum speed of approximately 1.5 m/s. In the present CALMET model, the vertical velocity is computed only by the orographic forcing and the initial guess wind filed is assumed to be quasi-nondivergent, which is incorrect under typhoon conditions as the vertical motion cannot be ignored in the inner core region. Therefore, the kinematic effects of terrain in CALMET can only be applied to atmospheric flows in stable conditions when the wind field is quasi-nondivergent. The present physical process of kinematic effects under very specific weather conditions needs to be improved in further study.

Acknowledgements This research was supported by the National Basic Research Program of China (No. 2015CB452806), the National Natural Science Foundation of China (Nos. 41805088, 41875080), Natural Science Foundation of Shanghai (No. 18ZR1449100), and Fundamental Research Foundation of Shanghai Typhoon Institute of the China Meteorological Administration (Nos. 2018JB05, 2019JB06).

References

Al-Yahyai S, Charabi Y, Gastli A (2010). Review of the use of Numerical Weather Prediction (NWP) models for wind energy assessment. Renew Sustain Energy Rev, 14(9): 3192–3198

Allwine K J, Whiteman C D (1985). MELSAR: A mesoscale air quality model for complex terrain. Volume 1—Overview, technical description and user's guide. Pacific Northwest Laboratory: Richland, Washington

Arakawa A, Jung J H, Wu C M (2011). Toward unification of the multiscale modeling of the atmosphere. Atmos Chem Phys, 11(8): 3731–3742

Black T L (1994). The new NMC mesoscale Eta model: description and forecast examples. Weather Forecast, 9(2): 265–278

Chen F, Dudhia J (2001). Coupling an advanced land surface hydrology model with the Penn State-NCAR MM5 modeling system. Part I: model implementation and sensitivity. Mon Weather Rev, 129(4): 569–585

GB/T 35237–2017. Specifications for Surface Meteorological Observation-automatic Observatrion. Beijing: China Standards Press, 2017 (in Chinese)

Gioli B, Gualtieri G, Busillo C, Calastrini F, Gozzini B, Miglietta F (2014). Aircraft wind measurements to assess a coupled WRF-CALMET mesoscale system. Meteorol Appl, 21(1): 117–128

González J A, Hernández-Garcés A, Rodriguez A, Saavedra S, Casares J J (2015). Surface and upper-air WRF-CALMET simulations assessment over a coastal and complex terrain area. Int J Environ Pollut, 57(3–4): 249–260

Goodin W R, Mcrae G J, Seinfeld J H (1980). An objective analysis technique for constructing three-dimensional urban-scale wind fields. J Appl Meteorol, 19(1): 98–108

Grell G A, Dudhia J, Stauffer D R (1995). A description of the fifth generation Penn State/NCAR mesoscale model (MM5). Tech Note NCAR/TN-398 + STR. NCAR: Boulder, CO

Holtslag A A M, Van Ulden A P (1983). A Simple scheme for daytime estimates of the surface fluxes from routine weather data. J Appl Meteorol, 22(4): 517–529

Horst T W, Doran J C (1986). Nocturnal drainage flow on simple slopes. Boundary-Layer Meteorol, 34(3): 263–286

Iacono M J, Delamere J S, Mlawer E J, Shephard M W, Clough S A, Collins W D (2008). Radiative forcing by long–lived greenhouse gases: calculations with the AER radiative transfer models. J Geophy Res-atmos, 113(D13)

Kain J S (2004). The Kain-Fritsch convective parameterization: an

update. J Appl Meteorol, 43(1): 170–181

Lam H, Kok M H, Shum K K Y (2012). Benefits from typhoons–the Hong Kong perspective. Weather, 67(1): 16–21

Lin Y L, Farley R D, Orville H D (1983). Bulk parameterization of the snow field in a cloud model. J Clim Appl Meteorol, 22(6): 1065–1092

Liu M K, Yocke M A (1980). Siting of wind turbine generators in complex terrain. J Energy, 4(1): 10–16

Lu Y X, Tang J P, Wang Y, Song L L (2012). Validation of near-surface winds obtained by a hybrid WRF/CALMET modeling system over a coastal island with complex terrain. J Trop Meteorol, 18(3): 284–296

Ludwig F L, Miller D K, Gallaher S G (2006). Evaluating a hybrid prognostic-diagnostic model that improves wind forecast resolution in complex coastal topography. J Appl Meteorol Climatol, 45(1): 155–177

Mahrt L (1982). Momentum balance of gravity flows. J Atmos Sci, 39 (12): 2701–2711

Mortensen N G, Landberg L (1993). Wind altas analysis and application program (WAsP) user's guide. Riso National Laboratory: Roskilde, Denmark

Pielke R A, Cotton W R, Walko R L, Tremback C J, Lyons W A, Grasso L D, Nicholls M E, Moran M D, Wesley D A, Lee T J, Copeland J H (1992). A comprehensive meteorological modeling system—RAMS. Meteorol Atmos Phys, 49(1–4): 69–91

Scire J S, Robe F R, Fernau M E, Yamartino R J (1998). A user's guide for the CALMET meteorological model (Version 5). Earth Tech Inc: Concord, MA

Skamarock W C, Klemp J B, Dudhia J, Gill D O, Barker D M, Duda M G, Huang X Y, Wang W, Powers J G (2008). A description of the advanced research WRF version 3. Tech Note NCAR/TN-475 + STR. NCAR: Boulder, CO.

Sukoriansky S, Galperin B, Perov V (2005). Application of a new spectral theory of stably stratified turbulence to the atmospheric boundary layer over sea ice. Boundary-Layer Meteorol, 117(2): 231–257

US EPA (2004). User's Guide for the AERMOD meteorological preprocessor (AERMET). EPA–454/B–03e002. U.S. Environmental Protection Agency: Research Triangle Park, NC

Wang W, Shaw W J, Seiple T E, Rishel J P, Xie Y (2008). An evaluation of a diagnostic wind model (CALMET). J Appl Meteorol Climatol, 47(6): 1739–1756

Wyngaard J C (2004). Toward numerical modeling in the "terra incognita". J Atmos Sci, 61(14): 1816–1826

Yim S H L, Fung J C H, Lau A K H, Kot S C (2007). Developing a high-resolution wind map for a complex terrain with a coupled MM5/CALMET system J Geophy Res-atmos, 112 (D5)

Ying M, Zhang W, Yu H, Lu X Q, Feng J X, Fan Y X, Zhu Y T, Chen D Q (2014). An overview of the China Meteorological Administration tropical cyclone database. J Atmos Ocean Technol, 31(2): 287–301

Zhao Y, Wang Y, Chen J, Huang H (2018). Numerical investigation on detailed structure of typhoon"Meranti"(2016) and extreme heavy rainfall event induced by it before and after landfall in Fujian. Torrential Rain Disa, 37(2): 135–148